Computational Materials Science 217 (2023) 111915

Contents lists available at ScienceDirect

Computational Materials Science

journal homepage: www.elsevier.com/locate/commatsci

Full Length Article

The effect of loading modes on the strain-dependent energy gap of CdTe quantum dots: A first-principles study

Jundiao Wang [a,b], Ronghao Shi [c], Pan Xiao [a,*]

[a] LNM, Institute of Mechanics, Chinese Academy of Sciences, Beijing 100190, China
[b] School of Engineering Sciences, University of Chinese Academy of Sciences, Beijing 100049, China
[c] School of Mechanical Engineering, Jiangsu University of Science and Technology, Zhenjiang, Jiangsu 212003, China

ARTICLE INFO

Keywords:
CdTe quantum dots
First-principles calculations
Strain-dependent energy gap
Loading modes

ABSTRACT

The strain-dependent photoluminescence (PL) properties of quantum dots (QDs) make them potential stress/strain sensing materials (SSM), especially for high-level stress states with nanometer and nanosecond resolution. However, the PL intensity and wavelength of QDs in experiments show nonlinear and non-monotonic dependence on applied strain/stress under some loading conditions, and the underlying mechanism needs microscopic investigations. In the work, first-principles calculations are performed on CdTe QDs of different sizes under three loading modes: hydrostatic compression (HC), shock compression (SC) and uniaxial compression (UC). Results show that the relationship between energy gap and applied strain is significantly dependent on the size of QD and the loading mode. Under the HC mode, the energy gap changes of CdTe QDs increase linearly with strain and the relationship is size-independent which is suitable for stress sensing. Under the SC mode, the energy gap also increases with strain, but the relationship is size-dependent. Under the UC mode, the relationship is negatively correlated for most cases and also shows significant size-dependence. LUMO/HOMO energies and electron cloud distributions are further investigated to find the key factor that controls the variations of energy gaps with strain under different loading modes. The findings help to understand the experimental phenomena of QDs under different loading modes, and also provide information for developing QDs-based SSMs.

1. Introduction

Quantum dots (QDs) are appealing nanoscale sensing materials due to their small sizes and promising photoluminescence (PL) behavior [1–5]. They have been reported to be used as electronic, photoluminescence, electrochemical and temperature sensors [6–8] in nanoscale. Recently, because of the strain-dependent PL responses, QDs are reported to be potential stress/strain sensing materials (SSM), especially for high-level stress state with nanometer and nanosecond resolution [9]. Experiments with different loading conditions have been carried out to investigate the stress/strain-dependent PL responses of QDs. Since QDs are usually prepared in solution state, hydrostatic compression (HC) is the commonly used loading condition in experiments [10–13]. As pressure increases, the blueshift of the PL spectra of QDs is observed [14–16] in HC experiments. Shock compression (SC) experiments on QDs embedded in a matrix are reported recently that a maximum value of blueshift for the PL spectra exists at a critical pressure, after which it becomes redshift due to the complicated coupling effect of stress state and temperature [9]. Fischer et al. [17] used AFM to perform uniaxial compression (UC) on a single QD, and the response in PL spectra is mainly blueshift, but redshift is also observed due to the different QDs orientations [18]. Although experimental studies on optical properties of QDs under different strain/stress conditions have been extensive, some basic questions still await in-depth investigation for the applications of QD-based SSM. First, the experimental results indicate that loading conditions with different strain triaxiality shows significant influence on the PL responses of QDs, which may lead to a non-monotonic transition from blueshift to redshift as strain increases. The non-monotonic response is not convenient for the design of QD-based SSM, so the underlying mechanism needs to be clarified. Second, as reported in experiments and calculations, the diameter [15,19], surface configuration [20,21] and strain state of QDs [17,18] will affect PL responses, then the degree of influence of these factors on the optic-mechanical behavior should be determined when designing QD-based SSM. However, it is rather difficult to precisely control these factors in experiments, and corresponding calculation is a great way to address the

* Corresponding author.
E-mail address: xiaopan@lnm.imech.ac.cn (P. Xiao).

https://doi.org/10.1016/j.commatsci.2022.111915
Received 7 September 2022; Accepted 10 November 2022
Available online 17 November 2022

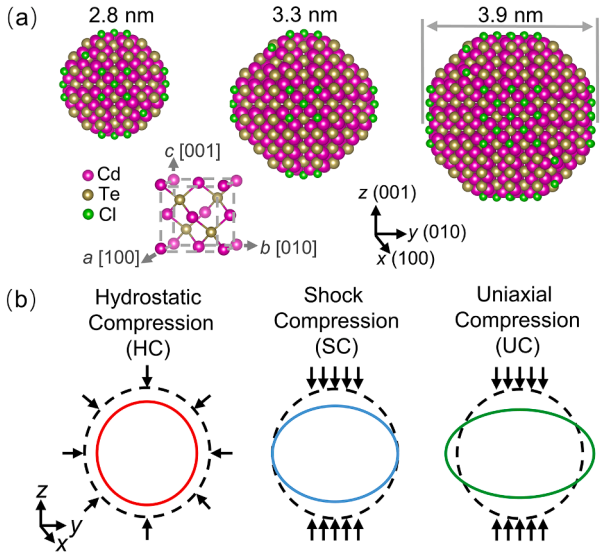

Fig. 1. (a) CdTe QD configurations with different diameters. (b) Illustration of different loading modes.

issues.

The strain-dependent PL response of QD is related to lattice deformation and energy gap changes. Specifically, the lattice of QD deforms when external strain is applied. The lattice deformation will lead to the change of energy gaps, and then the intensity and wavelength of PL will be changed accordingly. First-principles calculation is commonly used for understanding the mechanism related to strain-dependent energy gaps of QDs in microscopic level. In calculations, different forms of strain have been applied on QDs to explore the strain-related energy gaps, *e.g.*, UC [22,23], shear strain, biaxial strain and hydrostatic strain [19,24]. However, in order to understand the basic mechanism and rules for designing QD-based SSMs, a systematic and deep investigation regarding to the strain mode and size-dependent energy gaps of QDs should be carried out, especially for the QDs that have been reported for potential stress sensing applications. For example, CdTe QD has been used in hydrostatic and shock compression experiments [9,10,15] due to its advantages of simple and mature synthesis process and strong photoluminescence [25–27]. The PL intensity and wavelength of CdTe QDs in experiments show significant size and loading mode dependence, but it is not clear which is the main controlling factor to the different PL responses, and first-principles calculations regarding to the issue for CdTe QDs are less involved.

In the work, first-principles calculations are performed on CdTe QDs with different sizes and loading modes. The energies of lowest unoccupied molecular orbital (LUMO) and highest occupied molecular orbital (HOMO) and energy gaps are analyzed to elucidate the mechanism that controls the variation of PL wavelength with external strain. The fundamental reason of strain and size effect on the energy gap is further discussed by investigating the electron cloud distributions of the QDs at different strain states. The results are expected to help understand the experimental phenomena of QDs under different loading modes as well as provide microscopic information for developing QD-based SSMs.

2. Computational methods

The PL intensity and wavelength of QDs are dependent on size and external pressure [9–11], so the energy gap that controls the response of PL is usually calculated in first-principles calculations from the energy difference between HOMO and LUMO. Then, the relationship between energy gaps and strain can be calculated and analyzed for QDs with different sizes. Although there may be some deviation between experimental and calculated values of energy gaps, first-principles calculations can provide the same qualitative trend as a function of QD size and surface structure [28]. In the following, we focus on the energy difference between HOMO and LUMO which is one of the most important parameters that controls the responses of PL.

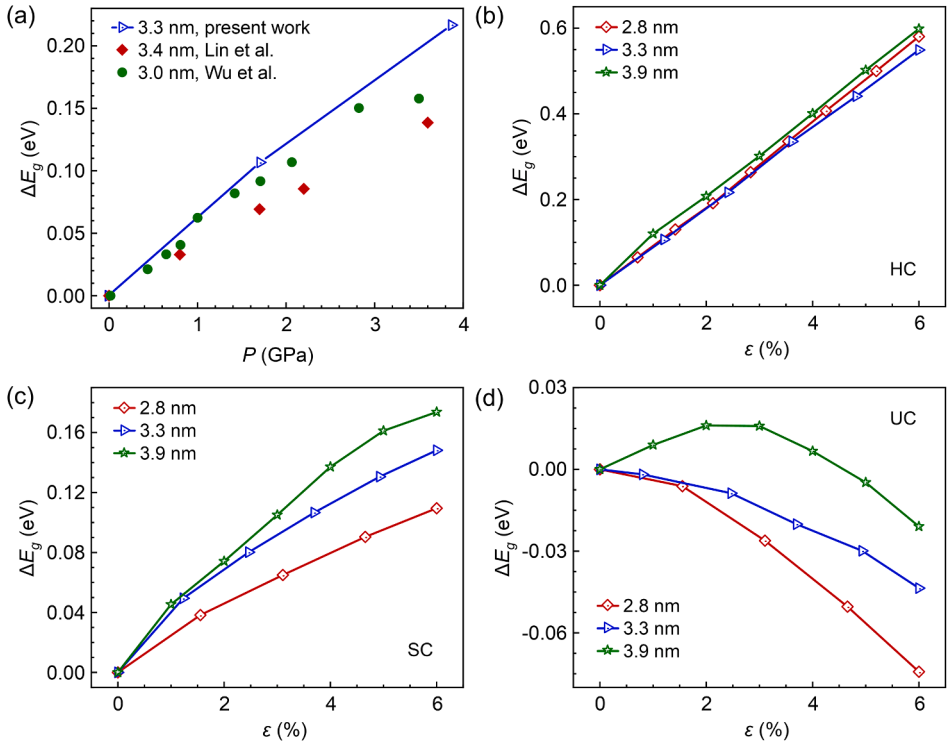

Fig. 2. (a) Variations of ΔE_g with pressure from calculations and experiments [10,12]. (b) – (c), variations of ΔE_g with strain for QDs of different sizes under loading conditions HC, SC and UC.

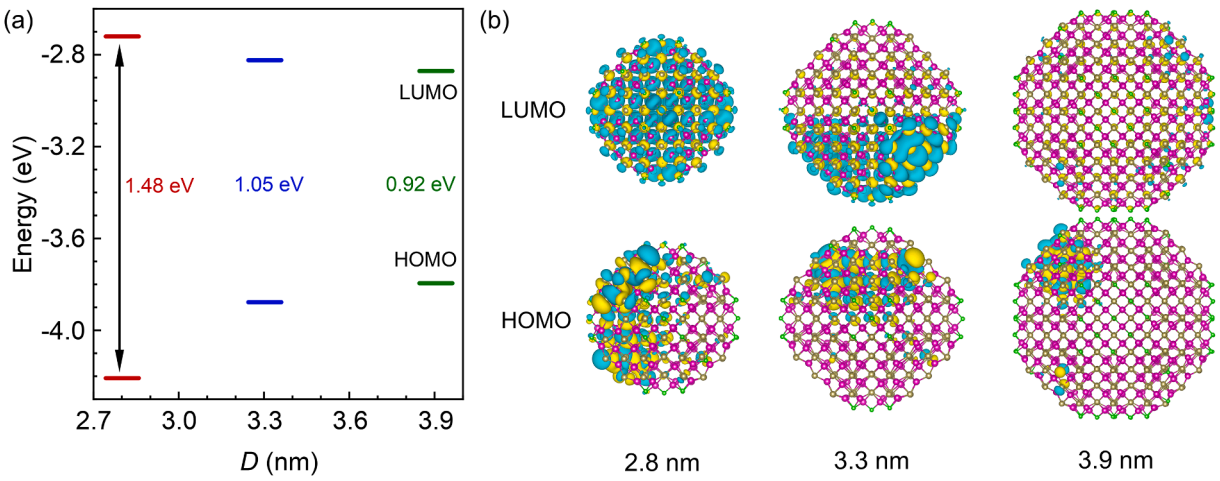

Fig. 3. (a) Variation of LUMO/HOMO energies with QD size at zero strain. (b) Wavefunction isosurfaces of LUMO/HOMO for QDs at zero strain. The colors yellow and cyan represent electron cloud isosurfaces with values of +0.005 and −0.005, respectively. (For interpretation of the references to colour in this figure legend, the reader is referred to the web version of this article.)

As shown in Fig. 1(a), CdTe QDs with diameters of 2.8, 3.3 and 3.9 nm of zinc-blende lattice (constant $a = 6.48$ Å) are calculated respectively. All the initial configurations are prepared by cutting from bulk CdTe lattice with all singly bonded atoms removed, and the resulting configurations have 321, 520 and 1131 atoms respectively. It is worth noting that all QDs are truncated with 26 facets: 6(1 0 0) + 8(1 1 1) + 12 (1 1 0), which is considered to be similar to the spherical shape of the QDs observed in experiments [20,29]. The exposed Cd atoms with two dangling bonds on the (1 0 0) facets can be passivated by Cl or oleic acid in experiments [29–31], and the addition of ligands has no effect on the energy gap [32]. For simplicity, Cl is used for passivation in the calculations. Since the total charge needs to be neutral in order to reduce the surface state [33], the number of additional Cl atoms is twice of excess Cd atoms.

Three loading modes with different strain triaxiality: HC, SC and UC, are applied to the prepared QDs for further calculations, as illustrated in Fig. 1(b). The HC loading mode is implemented by reducing distances between atomic positions and the shape center of QD proportionally. Both SC and UC are performed by applying compressive strain along the *z*-axis which agreements with the *c*-axis of lattice, while in the latter mode the Poisson's effect is considered. The Poisson's ratio is selected as 0.41 from experiments [34]. For convenience, the strain along the *z*-axis is used as the control variable for comparison, and the maximum strain in calculations is set as 6.0%.

The first-principles calculations are performed using CP2K/QUICKSTEP program [35] combined with Gaussian and plane wave methods. The generalized gradient approximation (GGA) [36] in a Perdew-Burke-Ernzerhof (PBE) formulation exchange correlation function is employed together with the norm-conserving Goedecker-Teter-Hutter (GTH) pseudopotentials. The short-range, molecularly optimized double-ζ single polarized basis set {DZVP-MOLOPT-SR-GTH} is used for Cd and Te elements, and the double-ζ single polarized basis set {DZVP-MOLOP-GTH} is used for Cl [37]. The optimization of geometries is achieved when atomic forces are below 2×10^{-5} Hartree/Bohr. Although the GGA can underestimate the energy gap, it can still provide a reliable structure with acceptable computational complexity [38], and has been widely used in energy and structure calculations for different QDs [28,39,40]. Therefore, the GGA function is selected to calculate the energy gaps for the CdTe QDs.

3. Results and discussion

3.1. Strain-dependent energy gaps

In order to check the validity of the calculation models and methods, variations of the energy gap with external loads from the first-principles calculations and experiments under HC are compared. Since the HC load is applied as strain in calculations, the equivalent pressure (P) is calculated from the famous Birch-Murnaghan (B-M) equation of state:

$$P = \frac{3B}{2}\left[\left(\frac{V_0}{V}\right)^{\frac{7}{3}} - \left(\frac{V_0}{V}\right)^{\frac{5}{3}}\right]\left\{1 + \frac{3}{4}(B' - 4)\left[\left(\frac{V_0}{V}\right)^{\frac{2}{3}} - 1\right]\right\} \quad (1)$$

where V_0 and V are the volume of QD at zero strain (ε_0) and a certain strain (ε) respectively; B and B' are bulk modulus and its derivative with respect to pressure, respectively. For the QD with a diameter of 3.3 nm, the parameters B and B' are 42 GPa and 6.4 respectively [41]. The difference between the energy gap at ε_0 and ε, is defined as ΔE_g which is used for the comparison. Variations of ΔE_g s as a function of P for QDs with similar diameters from calculations and experiments are presented in Fig. 2(a). Both results show the same variation trend, *i.e.*, the ΔE_g s increase with pressure. The calculated ΔE_g s are close to the experimental values when the pressure is<2.5 GPa after which the deviation increases. There are several reasons that lead to the deviation. First, the atomic deformation of the QD configuration imposed by the HC strain in calculations is not exactly the same as that induced by pressure in experiments, especially for the atoms near the surface. The difference in deformation will be more distinct when the pressure becomes larger [18]. However, it is hard to apply the same deformation field to QD configuration in calculations as that in experiments. Second, the parameters B and B' are functions of strain, here the constant values are used to approximately describe the evolution of ΔE_g with pressure. The approximation has been confirmed to be very close to the experimental results when pressure is small [18]. Nevertheless, the consistent trend of calculation and experiment indicates that the first-principles calculations can provide valuable and reliable results for the analysis of strain-dependent energy gaps.

The relationship between ΔE_g and ε (ΔE_g-ε) of QDs with different diameters under HC is presented in Fig. 2(b). The ΔE_g and ε are linearly and positively correlated for all the three QDs. Up to $\varepsilon = 6.0\%$, the ΔE_g s of the three sizes QDs increase to around 0.56 eV. Moreover, results of different sizes show very close ΔE_g, indicating that the ΔE_g-ε relationship is independent of the size of QDs under the HC condition. Fig. 2(c) shows the evolution of ΔE_g-ε for QDs with different sizes under SC. There

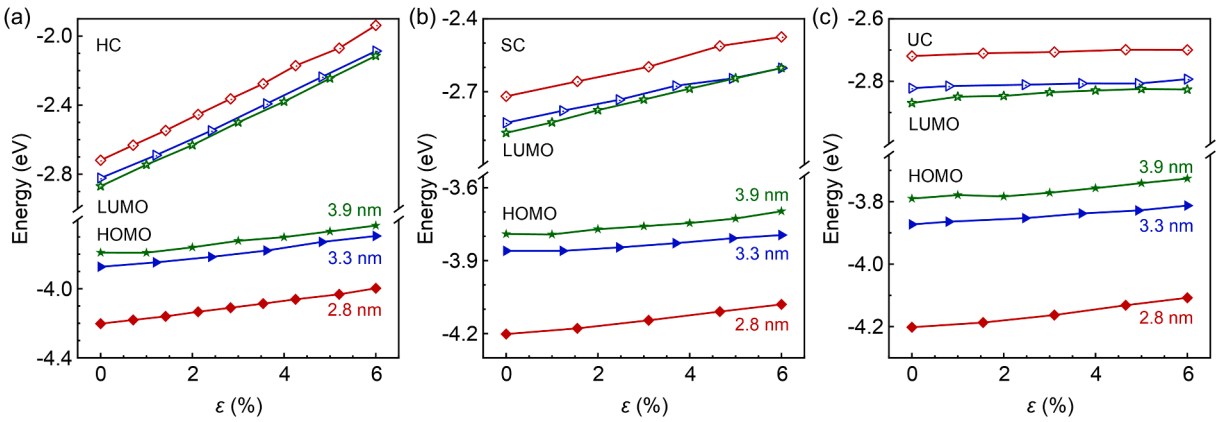

Fig. 4. Variation of LUMO/HOMO energies with ε for QDs with different sizes under the (a) HC, (b) SC and (c) UC loading modes.

is an obvious nonlinear positive correlation between ΔE_g and ε, which is in agreement with the previous work [34]. When ε is up to 6.0%, the ΔE_g of 2.8, 3.3 and 3.9 nm are 0.11, 0.15 and 0.17 eV, respectively, showing an increase with the diameter. Additionally, ΔE_g s of the QDs with the same size under SC are obviously smaller than that under HC at the same strain level. The variation of ΔE_g-ε of QDs with different sizes under UC is plotted in Fig. 2(d), and they show different trends. For QDs of 3.9 nm, ΔE_g increases with ε at the beginning, and then decreases when $\varepsilon >$ 2.0%. While for QDs of 2.8 and 3.3 nm, ΔE_g always decreases with ε which is in agreement with the results reported from Si QDs [22] and nano-diamonds [23]. For QDs of 2.8, 3.3 and 3.9 nm, the ΔE_g s at $\varepsilon =$ 6.0% are −0.07, −0.04 and −0.02 eV, respectively, behaving a positive size correlation, which is similar with that under SC. But it is clear that the ΔE_g of the same size QD under UC is the smallest among the three strain modes at the same strain level.

The ΔE_g-ε of QDs under the three loading modes from calculations shows distinct variation trends which means the strain triaxiality is one of the important factors that affects the strain-dependent PL responses. The ΔE_g is calculated based on the energies of LUMO and HOMO, which can be determined by the distribution of electron clouds of the wave-function isosurfaces. Therefore, the effect of strain on LUMO/HOMO energies as well as the distributions of electron cloud are further analyzed to investigate the size and strain dependence of ΔE_g.

3.2. Size and strain dependence of LUMO/HOMO energies

The LUMO/HOMO energies of QDs with different diameters at zero strain are shown in Fig. 3(a). Obviously, the gap between LUMO and HOMO, *i.e.*, E_g, significantly decreases with the diameter, which satisfies the quantum size effect. It can be found that the decrease of E_g with size is due to the decrease of LUMO energy and the increase of HOMO energy, while it is clear that the HOMO energy is the dominant factor because it is more sensitive to size than the LUMO energy, which will be explained further below.

The electron cloud states of LUMO/HOMO for each QD at zero strain are shown in Fig. 3(b). It can be seen that the LUMO shows anti-bonding character, *i.e.*, the charge primarily distributes in the vicinity of atoms. In contrast, the electron cloud of HOMO is mainly located in the intermediate regions of atoms and tends to form ionic or covalent bonds, indicating the bonding character [42]. Comparing the electron cloud of QDs with different sizes, it can be found that although the anti-bonding property of the LUMO is distributed throughout the whole QD, it still becomes weaken as the diameter increases. Therefore, the LUMO energies in Fig. 3(a) decreases with QD size. However, for the HOMO, the bonding state clearly tends to be localized on the (1 1 1) planes as the diameter increases, which indicates that the (1 1 1) planes with highly active cation- and anion-terminated surfaces are polar surfaces [43]. At the same time, it is also confirmed that the localized surface effect is almost dominant in larger QDs. Because of the surface-localized HOMO state, electrons are more likely to absorb photon energy and realize transition, which leads to the increased of HOMO energy in Fig. 3(a). The surface localization of HOMO state is also the reason why it is more sensitive to the diameter of QD than LUMO state.

Table 1
Deformation potentials of LUMO/HOMO energies with strain for different sizes of QDs under the three strain modes.

	D (nm)	α_{LU}(eV)	α_{HO}(eV)
HC	2.8	0.129	0.034
	3.3	0.123	0.031
	3.9	0.126	0.028
SC	2.8	0.042	0.021
	3.3	0.037	0.012
	3.9	0.046	0.014
UC	2.8	0.003	0.016
	3.3	0.004	0.010
	3.9	0.011 ($0 < \varepsilon < 2.0\%$)0.005 ($2.0\% < \varepsilon < 6.0\%$)	0.003 ($0 < \varepsilon < 2.0\%$)0.011 ($2.0\% < \varepsilon < 6.0\%$)

The strain-dependent LUMO/HOMO energies under different loading modes are plotted in Fig. 4. Additionally, the deformation potentials of LUMO and HOMO energies with strain are further calculated by fitting equations for quantitative analysis of the variation of orbital energies [44,45]:

$$\begin{cases} E_{LU} = E^0_{LU} + \alpha_{LU}\varepsilon \\ E_{HO} = E^0_{HO} + \alpha_{HO}\varepsilon \end{cases} \quad (2)$$

where E_{LU} and E_{HO} are LUMO and HOMO energies at ε, respectively; E^0_{LU} and E^0_{HO} are LUMO and HOMO energies at initial strain ε_0, respectively; α_{LU} and α_{HO} are deformation potentials of LUMO and HOMO, respectively. All the fitted α_{LU} and α_{HO} are listed in Table 1. For the QD of 3.9 nm under UC, because of the non-monotonic relationship between orbital energies and strain, two deformation potentials are obtained by fitting the two linear segments before and after the turning point $\varepsilon =$ 2.0%.

For the case of HC as shown in Fig. 4(a), it is obvious that the LUMO is more sensitive to strain than the HOMO, which is also indicated by the α_{LU} and α_{HO} listed in Table 1. Therefore, the correlation of ΔE_g with ε under HC in Fig. 2(b) is mainly due to the change of LUMO, which is similar to the conclusions of other works [22,24]. Moreover, the relative differences between α_{LU} and α_{HO} for QDs of 2.8, 3.3 and 3.9 nm are 74%, 75% and 78%, respectively, and the small difference results in the coincidence of ΔE_g in Fig. 2(b). For the case of SC as shown in Fig. 4(b), the LUMO is also more sensitive to strain than the HOMO which leads to the positive correlation between ΔE_g and ε in Fig. 2(c). Moreover, the

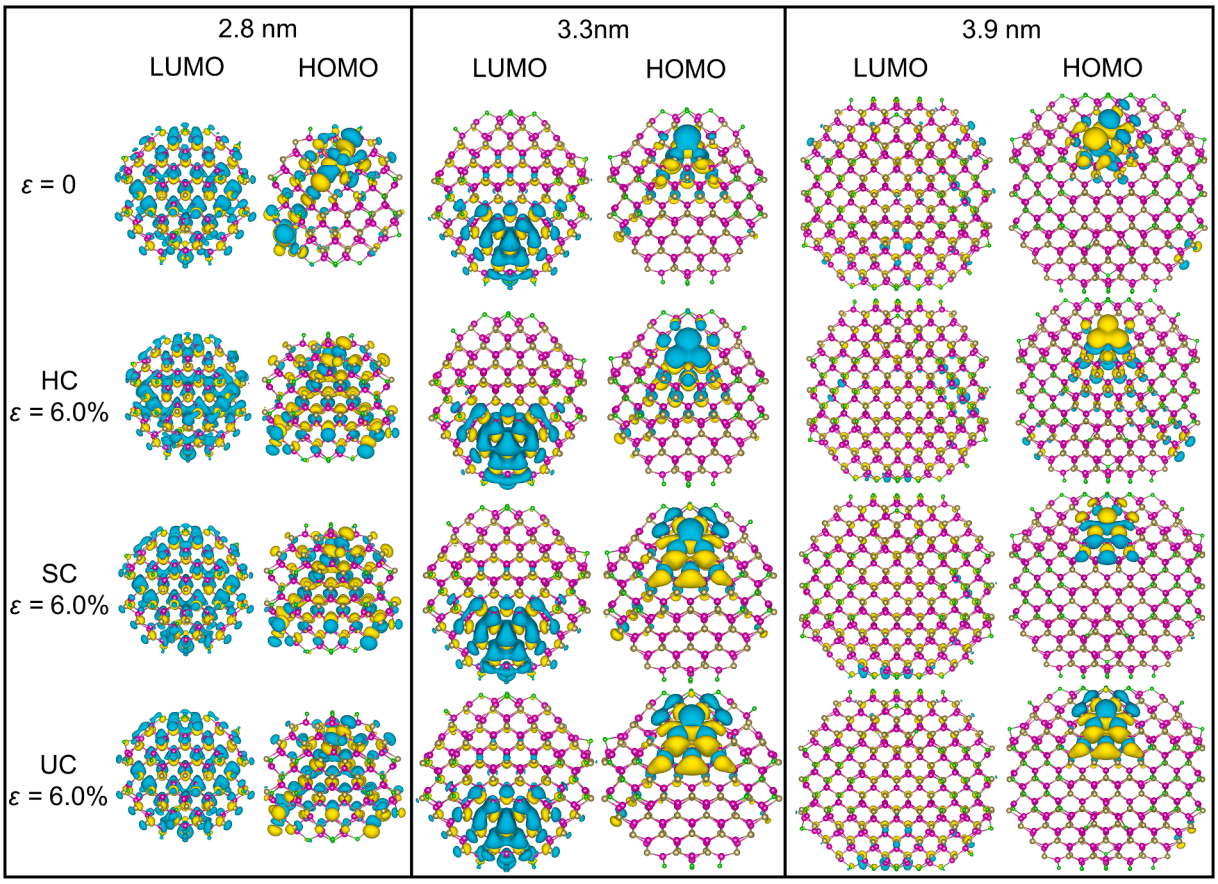

Fig. 5. Wavefunction isosurfaces of QDs with different sizes at $\varepsilon = 0$ and $\varepsilon = 6.0\%$ under the loading modes HC, SC and UC.

relative differences between α_{LU} and α_{HO} for the three QDs are 50%, 68% and 70%, respectively, which shows obvious size-dependence. For the case of UC in Fig. 4(c), the variation trends of LUMO and HOMO with strain are comparable which can be seen from the values of α_{LU} and α_{HO} in Table 1. The α_{LU} is smaller than α_{HO} for all the QDs at larger strain which leads to the negative growth of ΔE_g with ε at a larger strain level in Fig. 2(d). However, for the QD of 3.9 nm, the α_{LU} is larger than α_{HO} when $\varepsilon < 2.0\%$ which results in the increase in ΔE_g when $\varepsilon < 2.0\%$ in Fig. 2(d). Moreover, the relative differences between α_{LU} and α_{HO} for QDs with the size of 2.8, 3.3 and 3.9 nm are −433%, −150% and −120% ($2.0\% < \varepsilon < 6.0\%$), respectively, and resulting in the size dependence of the ΔE_g-ε relation in Fig. 2(d).

By comparing the deformation potentials of LUMO/HOMO energies in Table 1, as the loading mode changes from HC to UC, the strain for lateral confinement becomes weaker, and the α_{LU} and α_{HO} gradually decreases. Meanwhile, the relative differences between the α_{LU} and α_{HO} also decreases as the loading mode changes, so ΔE_g decreases accordingly for the same size QD at the same strain level in Fig. 2(b)-(d).

To further understand the strain and size dependence of LUMO and HOMO, the wavefunction isosurface plots for all the QDs at different strain states are shown in Fig. 5. The results can be analyzed from two aspects. First, for each QD with the same size, it can be found that the density of electron cloud of both LUMO and HOMO states at $\varepsilon = 6.0\%$ exhibits different degrees of enhancement in comparison with that at $\varepsilon = 0$ for all the three strain modes. The enhancement under the HC is the strongest, while it is the weakest under the UC. For the HC and SC strain modes, the interaction of nuclei-nuclei and nuclei-charge will be significantly enhanced with the reduction of atomic distance, which will lead to the enhancement of the anti-bonding state in LUMO and bonding state in HOMO, respectively, thus resulting in the increase in LUMO and HOMO energy in Fig. 4(a-b). For QDs under compressive strain, the nuclei-nuclei interaction is stronger than nuclei-charge interaction. Therefore, the α_{LU} is always larger than the α_{HO} for QDs with the same size as shown in Fig. 4(a-b). However, in comparison with HC, the application of SC strain only shortens the atomic distance along the z-axis which leads to the weaker nuclei-nuclei interaction, and it is the main reason why the α_{LU} of QD under SC is smaller than that under HC with the same size as discussed above. As for the UC strain mode, although the atomic distance along the z-axis decreases, the atomic distance in the xy plane increases due to the Poisson effect. As a result, the nucleus-electron attraction gradually plays the dominant role with the increase of strain, that is, the strain-induced bonding state of HOMO is gradually stronger than the anti-bonding state of LUMO, which causes the fact that the α_{LU} is smaller than the α_{HO} at a larger strain level in Fig. 4(c).

Second, for any strain mode, the LUMO and HOMO states of different sizes QDs respond differently to strain as shown in Fig. 5. For the HC mode, the density of electron cloud of LUMO state is significantly enhanced with stain due to its anti-bonding properties. The enhancement for both LUMO and HOMO decreases with increasing diameter which results in the size-independent relative difference between α_{LU} and α_{HO} in Fig. 4(a). For the SC and UC modes as shown in Fig. 5, the electron cloud of HOMO state appears to be shared by homogeneous atoms along the xy plane, indicating a tendency to form covalent bonds, which are not conducive to the transition of electrons. The electron cloud density that tends to form covalent bonds increases with diameter due to the surface localization of the HOMO state, which leads to a decrease in the enhancement of HOMO bonding state with diameter. As a result, the difference in the degree of enhancement between the strain-induced LUMO and HOMO increases with diameter. Therefore, the relative difference between α_{LU} and α_{HO} in Fig. 4(b-c) increases with diameter and leads to the size-related ΔE_g as shown in Fig. 2(c-d).

Additionally, the respond of HOMO states of different sizes QDs under the SC and UC stresses the fact that the surface deformation plays a more important role than the internal deformation [19].

4. Summary

In summary, first-principles calculations are performed to investigate the size and strain-dependent PL of CdTe QDs in three levels: variation of energy gaps, LUMO/HOMO energies and electron cloud distributions. In the first level, energy gaps of CdTe QDs under different loading modes are calculated in order to understand the wavelength change of PL. The results show that the variation of energy gaps with strain are strongly dependent on loading modes. Specifically, under the HC mode, the ΔE_g-ε curves of different sizes of QDs increase linearly and show size-independent. Under the SC mode, the ΔE_g also increases with ε, but the larger a QD is, the greater the slope of increase will be. Under the UC mode, the ΔE_g decreases with ε for most cases, and shows significant size dependence. Therefore, CdTe QDs are good SSM under the HC mode, while more calibration should be done if CdTe QDs were used as SSM under the SC and UC modes. In the second level, LUMO/HOMO energies are calculated to analyze the variation trend of energy gaps. The results show that HOMO energies of CdTe QDs have similar growth trend with strain under the three loading modes, while the LUMO energies are more sensitive to loading mode. The growth slope of LUMO energy is the largest under HC and smallest under UC, and it is the direct reason that leads to the different variation trends of energy gaps under different loading modes. In the third level, wavefunction isosurfaces from the first-principles calculations are used to analyze the electron clouds distributions of QDs at different strain states. Strain-induced antibonding state in LUMO and bonding state in HOMO as well as the surface localization of HOMO states are the basic factors that control the variation of LUMO and HOMO energies of QDs with different sizes and under different loading modes. The results can help to understand the experimental phenomena of QDs under different loading modes in greater depth, and also provide microscopic information for developing QDs-based SSMs.

Declaration of Competing Interest

The authors declare that they have no known competing financial interests or personal relationships that could have appeared to influence the work reported in this paper.

Data availability

No data was used for the research described in the article.

Acknowledgements

This work was supported by the National Natural Science Foundation of China (NSFC) (11790292 and 11672298) and the NSFC Basic Science Center Program for “Multiscale Problems in Nonlinear Mechanics” (11988102).

References

[1] I. Popescu, M. Hristache, S.S. Ciobanu, M.G. Barseghyan, J.A. Vinasco, A. L. Morales, A. Radu, C.A. Duque, Size or shape – What matters most at the nanoscale? Comput. Mater. Sci. 165 (2019) 13–22.
[2] X.u. Chen, X. Sun, W. Xu, G. Pan, D. Zhou, J. Zhu, H. Wang, X. Bai, B. Dong, H. Song, Ratiometric photoluminescence sensing based on Ti_3C_2 MXene quantum dots as an intracellular pH sensor, Nanoscale 10 (3) (2018) 1111–1118.
[3] P.A.S. Jorge, M. Mayeh, R. Benrashid, P. Caldas, J.L. Santos, F. Farahi, Quantum dots as self-referenced optical fibre temperature probes for luminescent chemical sensors, Meas. Sci. Technol. 17 (5) (2006) 1032–1038.
[4] M.F. Frasco, N. Chaniotakis, Semiconductor quantum dots in chemical sensors and biosensors, Sensors 9 (9) (2009) 7266–7286.
[5] J.A. Thomas, Optical imaging probes for biomolecules: an introductory perspective, Chem. Soc. Rev. 44 (14) (2015) 4494–4500.
[6] R. Liang, R. Tian, W. Shi, Z. Liu, D. Yan, M. Wei, D.G. Evans, X. Duan, A temperature sensor based on CdTe quantum dots–layered double hydroxide ultrathin films via layer-by-layer assembly, Chem. Commun. 49 (10) (2013) 969–971.
[7] Z.S. Hosseini, A. Iraji zad, M.A. Ghiass, S. Fardindoost, S. Hatamie, A new approach to flexible humidity sensors using graphene quantum dots, J. Mater. Chem. C. 5 (35) (2017) 8966–8973.
[8] N. Sohal, B. Maity, S. Basu, Recent advances in heteroatom-doped graphene quantum dots for sensing applications, RSC Adv. 11 (41) (2021) 25586–25615.
[9] Z. Kang, A.A. Banishev, G. Lee, D.A. Scripka, J. Breidenich, P. Xiao, J. Christensen, M. Zhou, C.J. Summers, D.D. Dlott, N.N. Thadhani, Exploration of CdTe quantum dots as mesoscale pressure sensors via time-resolved shock-compression photoluminescent emission spectroscopy, J. Appl. Phys. 120 (4) (2016), 043107.
[10] Y.C. Lin, Water-soluble CdTe nanocrystals under high pressure, in: D.L. Huffaker, H. Eisele (Eds.), Quantum Dots Nanostructures Synth. Charact. Model. XII, 9373 (2015) 93730L.
[11] P.T.C. Freire, M.A. Araújo Silva, V.C.S. Reynoso, A.R. Vaz, V. Lemos, Pressure Raman scattering of CdTe quantum dots, Phys. Rev. B. 55 (11) (1997) 6743–6746.
[12] F. Wu, J.M. Zaug, C.E. Young, J.Z. Zhang, Pressure-induced phase transition in thiol-capped CdTe nanoparticles, J. Nanosci. Nanotechnol. 8 (12) (2008) 6528–6532.
[13] B. Li, W. Liu, X. Zhu, S. Lin, Y. Yang, Q. Yang, P. Jin, Pressure-dependent photoluminescence of CdSe/ZnS quantum dots: critical point of different pressure regimes, Phys. Lett. A. 383 (13) (2019) 1483–1486.
[14] H. Liu, X. Zhao, X. Yang, Y. Wang, M. Wu, J. Jiang, G. Wu, K. Yuan, L. Sui, B. Zou, Piezochromic luminescence in all-inorganic core–shell InP/ZnS nanocrystals via pressure-modulated strain engineering, Nanoscale Horiz. 5 (8) (2020) 1233–1239.
[15] Y.C. Lin, W.C. Chou, A.S. Susha, S.V. Kershaw, A.L. Rogach, Photoluminescence and time-resolved carrier dynamics in thiol-capped CdTe nanocrystals under high pressure, Nanoscale 5 (8) (2013) 3400–3405.
[16] P. łach, G. Karczewski, P. Wojnar, T. Wojtowicz, M.G. Brik, A. Kamińska, A. Reszka, B.J. Kowalski, A. Suchocki, Pressure coefficients of the photoluminescence of the IIVI semiconducting quantum dots grown by molecular beam epitaxy, J. Lumin. 132 (6) (2012) 1501–1506.
[17] T. Fischer, S. Stöttinger, G. Hinze, A. Bottin, N. Hu, T. Basché, Single semiconductor nanocrystals under compressive stress: reversible tuning of the emission energy, Nano Lett. 17 (3) (2017) 1559–1563.
[18] C.D. Grant, J.C. Crowhurst, S. Hamel, A.J. Williamson, N. Zaitseva, Anomalous photoluminescence in CdSe quantum-dot solids at high pressure due to nonuniform stress, Small 4 (6) (2008) 788–794.
[19] X.H. Peng, S. Ganti, A. Alizadeh, P. Sharma, S.K. Kumar, S.K. Nayak, Strain-engineered photoluminescence of silicon nanoclusters, Phys. Rev. B. 74 (3) (2006), 035339.
[20] Y. Zhao, Y.H. Kim, M.H. Du, S. Zhang, First-principles prediction of icosahedral quantum dots for tetravalent semiconductors, Phys. Rev. Lett. 93 (1) (2004), 015502.
[21] H.N. Du, J. Li, H. Li, Y.Y. Shen, C.X. Xu, Influence of quantum dot shape on the formation energy of boron dopants in silicon, J. Appl. Phys. 128 (5) (2020), 055102.
[22] X. Jiang, J. Zhao, X. Jiang, Tuning the electronic and optical properties of hydrogen-terminated Si nanocluster by uniaxial compression, J. Nanoparticle Res. 14 (4) (2012) 818.
[23] X. Jiang, J. Zhao, C. Zhuang, B. Wen, X. Jiang, Mechanical and electronic properties of ultrathin nanodiamonds under uniaxial compressions, Diam. Relat. Mater. 19 (1) (2010) 21–25.
[24] X.H. Peng, A. Alizadeh, N. Bhate, K.K. Varanasi, S.K. Kumar, S.K. Nayak, First-principles investigation of strain effects on the energy gaps in silicon nanoclusters, J. Phys. Condens. Matter. 19 (26) (2007), 266212.
[25] Z. Deng, Y. Zhang, J. Yue, F. Tang, Q. Wei, Green and orange CdTe quantum dots as effective pH-sensitive fluorescent probes for dual simultaneous and independent detection of viruses, J. Phys. Chem. B. 111 (41) (2007) 12024–12031.
[26] J. Bao, M.G. Bawendi, A colloidal quantum dot spectrometer, Nature 523 (7558) (2015) 67–70.
[27] A. Badawi, N. Al-Hosiny, S. Abdallah, S. Negm, H. Talaat, Tuning photocurrent response through size control of CdTe quantum dots sensitized solar cells, Sol. Energy 88 (2013) 137–143.
[28] F.A. Reboredo, L. Pizzagalli, G. Galli, Computational engineering of the stability and optical gaps of SiC quantum dots, Nano Lett. 4 (5) (2004) 801–804.
[29] O. Voznyy, E.H. Sargent, Atomistic model of fluorescence intermittency of colloidal quantum dots, Phys. Rev. Lett. 112 (15) (2014), 157401.
[30] O. Voznyy, S.M. Thon, A.H. Ip, E.H. Sargent, Dynamic trap formation and elimination in colloidal quantum dots, J. Phys. Chem. Lett. 4 (6) (2013) 987–992.
[31] N.C. Anderson, M.P. Hendricks, J.J. Choi, J.S. Owen, Ligand exchange and the stoichiometry of metal chalcogenide nanocrystals: spectroscopic observation of facile metal-carboxylate displacement and binding, J. Am. Chem. Soc. 135 (49) (2013) 18536–18548.
[32] S. Kilina, K.A. Velizhanin, S. Ivanov, O.V. Prezhdo, S. Tretiak, Surface ligands increase photoexcitation relaxation rates in CdSe quantum dots, ACS Nano 6 (7) (2012) 6515–6524.
[33] O. Voznyy, Mobile surface traps in CdSe nanocrystals with carboxylic acid ligands, J. Phys. Chem. C. 115 (32) (2011) 15927–15932.
[34] P. Xiao, F. Ke, Y. Bai, M. Zhou, Deformation-induced blueshift in emission spectrum of CdTe quantum dot composites, Compos. Part B Eng. 120 (2017) 54–62.

[35] J. Hutter, M. Iannuzzi, F. Schiffmann, J. Vandevondele, Cp2k: Atomistic simulations of condensed matter systems, Wiley Interdiscip. Rev. Comput. Mol. Sci. 4 (1) (2014) 15–25.
[36] J.P. Perdew, K. Burke, M. Ernzerhof, Generalized gradient approximation made simple, Phys. Rev. Lett. 77 (18) (1996) 3865–3868.
[37] J. VandeVondele, J. Hutter, Gaussian basis sets for accurate calculations on molecular systems in gas and condensed phases, J. Chem. Phys. 127 (11) (2007), 114105.
[38] W.L. Ding, X.L. Peng, Z.Z. Sun, Z.S. Li, The electron injection rate in CdSe quantum dot sensitized solar cells: from a bifunctional linker and zinc oxide morphology, Nanoscale 9 (43) (2017) 16806–16816.
[39] S.K. Medeiros, E.L. Albuquerque, F.F. Maia, E.W.S. Caetano, V.N. Freire, Electronic and optical properties of $CaCO_3$ calcite, and excitons in Si@$CaCO_3$ and $CaCO_3$@SiO_2 core-shell quantum dots, J. Phys. D. Appl. Phys. 40 (18) (2007) 5747–5752.
[40] A. Franceschetti, Structural and electronic properties of PbSe nanocrystals from first principles, Phys. Rev. B - Condens. Matter Mater. Phys. 78 (7) (2008) 1–6.
[41] M.I. McMahon, R.J. Nelmes, N.G. Wright, D.R. Allan, Phase transitions in CdTe to 5 GPa, Phys. Rev. B. 48 (22) (1993) 16246–16251.
[42] R. Peköz, Ş. Erkoç, A density functional theory study on the structures and energetics of Cd_mTe_n clusters ($m+n\leqslant 6$), Comput. Mater. Sci. 45 (4) (2009) 912–920.
[43] H. Liu, X. Yang, K. Wang, Y. Wang, M. Wu, X. Zuo, W. Yang, B. Zou, Pressure-induced multidimensional assembly and sintering of $cuins_2$ nanoparticles into lamellar nanosheets with band gap narrowing, ACS Appl. Nano Mater. 3 (3) (2020) 2438–2446.
[44] M. Zieliński, M. Korkusiński, P. Hawrylak, Atomistic tight-binding theory of multiexciton complexes in a self-assembled InAs quantum dot, Phys. Rev. B. 81 (8) (2010), 085301.
[45] J. Shi, Y. Ou, M.A. Migliorato, H. Wang, H. Li, Y. Zhang, Y. Gu, M. Zou, Tuning the electronic structure of GeC/WS_2 van der Waals heterostructure by electric field and strain: a first principles study, Comput. Mater. Sci. 160 (2019) 301–308.